Numerical simulation of compressible flows with immersed boundaries using Discontinuous Galerkin methods

Bachelor thesis by Simone Stange, Department of Computational Engineering
March 15, 2016
Supervisors: Prof. Dr.-Ing. Martin Oberlack, Dr.-Ing. Björn Müller
Department for Fluid Dynamics

TECHNISCHE
UNIVERSITÄT
DARMSTADT

ce

fdy

Simone Katharina Stange
Matrikelnummer: 2012232
Studiengang: B.Sc. Computational Engineering

Bachelorarbeit
Thema: Numerical simulation of compressible flows with immersed boundaries using Discontinuous Galerkin methods

Eingereicht: March 15, 2016

Betreuer: Dr.-Ing. Björn Müller

Prof. Dr.-Ing. Martin Oberlack
Fachgebiet für Strömungsdynamik
Fachbereich Maschinenbau
Technische Universität Darmstadt
Otto-Berndt-Str. 2
64287 Darmstadt

1 Declaration of Academic Integrity

Thesis Statement pursuant to § 22 paragraph 7 of APB TU Darmstadt

I herewith formally declare that I have written the submitted thesis independently. I did not use any outside support except for the quoted literature and other sources mentioned in the paper. I clearly marked and separately listed all of the literature and all of the other sources which I employed when producing this academic work, either literally or in content. This thesis has not been handed in or published before in the same or similar form.
In the submitted thesis the written copies and the electronic version are identical in content.

Date: Signature:

Abstract

Informationen zu Inhalten der Zusammenfassung entnehmen Sie bitte Kapitel 6.1 des Skripts zur Veranstaltung *Wissenschaftliches Arbeiten und Schreiben für Maschinenbau-Studierende*.

Lorem ipsum dolor sit amet, consectetuer adipiscing elit. Etiam lobortis facilisis sem. Nullam nec mi et neque pharetra sollicitudin. Praesent imperdiet mi nec ante. Donec ullamcorper, felis non sodales commodo, lectus velit ultrices augue, a dignissim nibh lectus placerat pede. Vivamus nunc nunc, molestie ut, ultricies vel, semper in, velit. Ut porttitor. Praesent in sapien. Lorem ipsum dolor sit amet, consectetuer adipiscing elit. Duis fringilla tristique neque. Sed interdum libero ut metus. Pellentesque placerat. Nam rutrum augue a leo. Morbi sed elit sit amet ante lobortis sollicitudin. Praesent blandit blandit mauris. Praesent lectus tellus, aliquet aliquam, luctus a, egestas a, turpis. Mauris lacinia lorem sit amet ipsum. Nunc quis urna dictum turpis accumsan semper.

Lorem ipsum dolor sit amet, consectetuer adipiscing elit. Etiam lobortis facilisis sem. Nullam nec mi et neque pharetra sollicitudin. Praesent imperdiet mi nec ante. Donec ullamcorper, felis non sodales commodo, lectus velit ultrices augue, a dignissim nibh lectus placerat pede. Vivamus nunc nunc, molestie ut, ultricies vel, semper in, velit. Ut porttitor. Praesent in sapien. Lorem ipsum dolor sit amet, consectetuer adipiscing elit. Duis fringilla tristique neque. Sed interdum libero ut metus. Pellentesque placerat. Nam rutrum augue a leo. Morbi sed elit sit amet ante lobortis sollicitudin. Praesent blandit blandit mauris. Praesent lectus tellus, aliquet aliquam, luctus a, egestas a, turpis. Mauris lacinia lorem sit amet ipsum. Nunc quis urna dictum turpis accumsan semper.

Lorem ipsum dolor sit amet, consectetuer adipiscing elit. Etiam lobortis facilisis sem. Nullam nec mi et neque pharetra sollicitudin. Praesent imperdiet mi nec ante. Donec ullamcorper, felis non sodales commodo, lectus velit ultrices augue, a dignissim nibh lectus placerat pede. Vivamus nunc nunc, molestie ut, ultricies vel, semper in, velit. Ut porttitor. Praesent in sapien. Lorem ipsum dolor sit amet, consectetuer adipiscing elit. Duis fringilla tristique neque. Sed interdum libero ut metus. Pellentesque placerat. Nam rutrum augue a leo. Morbi sed elit sit amet ante lobortis sollicitudin. Praesent blandit blandit mauris. Praesent lectus tellus, aliquet aliquam, luctus a, egestas a, turpis. Mauris lacinia lorem sit amet ipsum. Nunc quis urna dictum turpis accumsan semper.

Contents

2 Introduction

The chair of fluid dynamics of the technical university Darmstadt mainly deals with research in fluid mechanical problems, e.g. multiphase flows, turbulence or thermodynamics. In recent years they have been developing a BoSSS, a software using a Runge-Kutta Discontinous Galerkin (RKDG) method for simulation of both incompressible and compressible Navier-Stokes, that is highly parallelizable and allows distinct grid types and dimensions (2-dimensional (2D), 3-dimensional (3D)) and arbitrarily defined polynomial order.

In this thesis we will concentrate on a 2D grid that is based on an IBM. The BoSSS code in combination with IBM firstly needs to be validated concerning incompressible Navier Stokes, which will be done in 6, thus giving a basis for examining the calculations of the compressible Navier Stokes case.

For both cases we will study the 2D flow around a cylinder for different mesh sizes and polynomial degrees, also varying the Reynolds number as we are studying the compressible viscous flow in 7.

In order to be able to conceive the results which we will get by our simulations, I will first give some theory about the fundamental equations in 3, the RKDG method in **??** and the grid type based on the IBM in 5. @TODO: what has been done already?

3 Fundamentals

3.1 Essential Equations

In the following we will introduce the essential equations that form the basis of all methods and results discussed in this thesis.

3.1.1 Equations of State

First, I will enumerate the basic thermodynamic equations of state that describe the relations between the specific inner energy e, the local temperature T, the specific enthalpy $\bar{h}$, the pressure $p = p(\rho, e)$, the density ρ and the specific entropy s. Assuming that all material parameters are constant, we receive

$$e = c_v T \tag{3.1}$$

$$\bar{h} = c_p T = e + \frac{p}{\rho} \tag{3.2}$$

with the material parameters c_p and c_v as specific heat capacities at constant pressure and volume, respectively. Using these relations, we can define the heat capacity ratio

$$\gamma = \frac{c_p}{c_v} = \frac{\bar{h}}{e}, \tag{3.3}$$

e.g. $\gamma = 1.4$ for standard air.

Another essential equation is the relation for the specific entropy

$$T\,ds = de + p\,d\rho^{-1}. \tag{3.4}$$

3.1.2 Ideal Gas Law

The equations of state mentioned above are not yet complete as there is missing a law for the pressure $p = p(\rho, e)$. In this thesis we will confine ourselves to the ideal gas law as we are only

modelling standard air($\gamma = 1.4$).
The ideal gas law is defined as

$$p = (\gamma - 1)\rho e \tag{3.5}$$

with $\rho e \in \mathbb{R}^+$ denoting the inner energy.

The speed of sound is defined as

$$a = \sqrt{\left.\frac{\partial p}{\partial \rho}\right|_s}. \tag{3.6}$$

Using this definition combined with the ideal gas law and an equation for the change of entropy as can be read in [1] leads to the useful relations

$$a^2 = \gamma \frac{p}{\rho} \tag{3.7}$$

$$\frac{p}{\rho^\gamma} = \text{const.} \tag{3.8}$$

3.1.3 Navier-Stokes Equations

The compressible Navier-Stokes equations (CNS) in conservative forms read as

$$\frac{\partial \mathbf{U}}{\partial t} + \frac{\partial \mathbf{F}_i^c(\mathbf{U})}{\partial x_i} - \frac{\partial \mathbf{F}_i^v(\mathbf{U}, \nabla \mathbf{U})}{\partial x_i} = \mathbf{B}, \tag{3.9}$$

with the denotations $\mathbf{U}$ as the conserved flow variables, $\mathbf{F}_i^c$ and $\mathbf{F}_i^v$ as the convective and viscous fluxes and $\mathbf{B}$ as source terms:

$$\mathbf{U} = \begin{pmatrix} \rho \\ \rho v_j \\ \rho E \end{pmatrix}, \quad \mathbf{F}_i^c = \begin{pmatrix} \rho v_i \\ \rho v_i v_j + p\delta_{ij} \\ v_i(\rho E + p) \end{pmatrix}, \quad \mathbf{F}_i^v = \begin{pmatrix} 0 \\ \tau_{ij} \\ \tau_{ij} + q_i \end{pmatrix}, \quad \mathbf{B} = \begin{pmatrix} 0 \\ \rho F_j \\ \rho F_j v_j + Q_i \end{pmatrix}. \tag{3.10}$$

In addition to the denotations in 3.1.1 we have F_j as body forces, Q_i as heat sources, the viscous stress tensor

$$\tau_{ij} = \mu \left[\left(\frac{\partial v_i}{\partial x_j} + \frac{\partial v_j}{\partial x_i} \right) - \frac{2}{3} \frac{\partial v_k}{\partial x_k} \delta_{ij} \right] \tag{3.11}$$

with the dynamic viscosity μ and the heat flux q_i modelled using Fourier's Law

$$q_i = k \frac{\partial T}{\partial x_i}. \tag{3.12}$$

Euler Equations

Regarding only compressible inviscid flow, the viscous fluxes and the source terms dissolve ($\mathbf{F}_i^\nu = \mathbf{B} = \mathbf{0}$) and the Navier-Stokes equations simplify to

$$\frac{\partial \mathbf{U}}{\partial t} + \frac{\partial \mathbf{F_x^c(U)}}{\partial x} + \frac{\partial \mathbf{F_y^c(U)}}{\partial y} = 0. \tag{3.13}$$

3.2 Dimensionless Measures

For it is much easier to handle dimensionless PDEs, we will introduce some dimensionless measures. In order to derive these, we need some reference quantities: L_∞ as a reference length, a reference velocity V_∞, reference density ρ_∞, reference volume force g_∞, reference viscosity μ_∞, reference thermal conductivity coefficient k_∞ and the gas constant R @TODO: Krämer-Eis zitieren. All other reference quantities can be derived from those. In the following all dimensionless quantities will be marked with an asterisk ()*:

$$t^* = \frac{V_\infty}{L_\infty} \cdot t, \quad x_i^* = \frac{1}{L} \cdot x_i, \quad v_i^* = \frac{1}{V_\infty} \cdot v_i, \quad \rho^* = \frac{1}{\rho_\infty} \cdot \rho, \quad p^* = \frac{1}{\rho_\infty V_\infty^2} \cdot p, \quad (3.14)$$

$$\mu^* = \frac{1}{\mu_\infty} \cdot \mu, \quad k^* = \frac{1}{k_\infty} \cdot k, \quad T^* = \frac{R}{V_\infty^2} \cdot T, \quad F_j^* = \frac{1}{g_\infty} \cdot F_j, \quad \rho E^* = \frac{1}{\rho_\infty V_\infty^2} \cdot \rho E,$$

$$Q_i^* = \frac{L}{V_\infty^3} \cdot Q.$$

In order to derive the non-dimensional form of the CNS, we also need the dimensionless operators:

$$\frac{\partial}{\partial t} = \frac{\partial t^*}{\partial t} \frac{\partial}{\partial t^*} = \frac{V_\infty}{L} \frac{\partial}{\partial t^*}, \tag{3.15}$$

$$\frac{\partial}{\partial x_i} = \frac{\partial x_i^*}{\partial x_i} \frac{\partial}{\partial x_i^*} = \frac{1}{L} \frac{\partial}{\partial x_i^*}, \tag{3.16}$$

$$\nabla = \frac{1}{L} \nabla^*. \tag{3.17}$$

3.2.1 Non-dimensional Ideal Gas Law

For a closed system of equations we have to use the ideal gas law in dimensionless form:

$$p^* = \rho^*(\gamma - 1)e^* \tag{3.18}$$

$$= (\gamma - 1)\left(\rho E^* - \frac{1}{2}\rho^* \mathbf{v}^{*2}\right). \tag{3.19}$$

3.2.2 Dimensionless Navier-Stokes Equations

As we now have all required measures and operator we can use them to define the dimensionless relations @TODO: zahlen erklären

Reynolds Number $\quad \mathrm{Re} = \dfrac{\rho_\infty V_\infty L}{\mu_\infty} \propto \dfrac{\text{inertia forces}}{\text{viscous forces}}$,

Froude Number $\quad \mathrm{Fr} = \dfrac{V_\infty}{\sqrt{gL}} \propto \dfrac{\text{body inertia}}{\text{gravitational forces}}$,

Prandtl Number $\quad \mathrm{Pr} = \dfrac{\mu_\infty c_p}{k_\infty} \propto \dfrac{\text{viscous diffusion rate}}{\text{thermal diffusion rate}}$.

Putting all together we receive the dimensionless Navier-Stokes equations. As they only depend on non-dimensional quantities we can drop the asterisk:

$$\frac{\partial \mathbf{U}}{\partial t} + \frac{\partial \mathbf{F}_i^c(\mathbf{U})}{\partial x_i} - \frac{\partial \mathbf{F}_i^v(\mathbf{U}, \nabla \mathbf{U})}{\partial x_i} = \mathbf{B} \tag{3.20}$$

with the dimensionless fluxes

$$\mathbf{F}_i^c = \begin{pmatrix} \rho v_i \\ \rho v_i v_j + p\delta_{ij} \\ v_i(\rho E + p) \end{pmatrix}, \quad \mathbf{F}_i^v = \frac{1}{\mathrm{Re}} \begin{pmatrix} 0 \\ \tau_{ij} \\ \tau_{ij}v_j + \dfrac{\gamma}{\mathrm{Pr}(\gamma-1)}q_i \end{pmatrix}, \quad \mathbf{B} = \frac{1}{\mathrm{Fr}^2} \begin{pmatrix} 0 \\ \rho F_j \\ \rho F_j v_j \end{pmatrix} + \begin{pmatrix} 0 \\ 0 \\ Q_j \end{pmatrix}. \tag{3.21}$$

4 The Runge-Kutta Discontinous Galerkin Method

This thesis deals with the software BoSSS that uses a RKDG method for the numerical approximation of compressible flows. The RKDG method is split into the Discontinous Galerkin (DG) method for space discretization and the Runge-Kutta (RK) method as an explicit time discretization. By using an explicit time-marching algorithm, the parallelization is made much easier.

In the following sections we will study the DG and RK methods separately considering simple examples and using the same notation as in [1].

4.1 DG Space Discretization

First, we will study the DG method which can be seen as combination of the finite volume method (FVM) and the finite element method (FEM). It aims at combining the advantages of both methods, namely high-order accuracy and hp-adaptivity (FEM) as well as conservativity (FVM), thus allowing the computation of higher order solutions with adjustable order on each element on a conservative grid. The main concept of the DG method is visualised in 4.1.

(a) First order FEM   (b) Zeroth order DG (FVM)   (c) First order DG
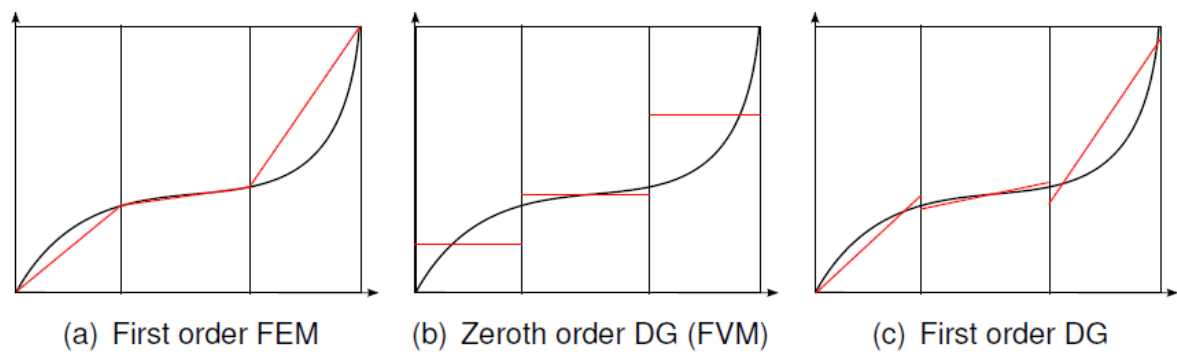
Figure 4.1.: Comparison of FEM, FVM and DG @TODO: cite fdy vortrag

As a simple example that we can use to derive the DG formulation we will consider the scalar conservation law

$$\frac{\partial c}{\partial t} + \nabla \cdot \boldsymbol{f}(c) = 0 \tag{4.1}$$

for the concentration $c = c(\boldsymbol{x}, t)$ with $\vec{x} \in \Omega \subset \mathbb{R}^D$ and $t \in \mathbb{R}_0^+$ and a smooth function $\boldsymbol{f} : \mathbb{R} \to \mathbb{R}^D$ that also contains suitable initial and boundary conditions.[1]

4.1.1 Weak Formulation

Our first step of the DG method will be transfering the partial differential equation (4.1) into a weak formulation. Priorly to this we need a discretization Ω_h of Ω consisting of a tesselation of cells $\{\mathcal{K}_i\}_{i=1,\dots,N}$, where h represents a measure for the size of the cells. Each cell $\mathcal{K}_i$ is of dimension D with an outward unit normal vector $\boldsymbol{n}$.

After having discretized our geometry, we now need a set of cell-local test functions $\{\Phi_{i,j}\}_{j=1,\dots,M}$ with $\Phi_{i,j} = \Phi_{i,j}(\boldsymbol{x}) : \mathbb{R}^D \to \mathbb{R}$ that forms the basis of polynomials $P_{\mathcal{K}_i}(P)$ with the maximum degree P.

In order to obtain the weak formulation we will now multiply equation (4.1) by $\Phi_{i,j}$, integrate over a cell $\mathcal{K}_i$ and then integrate by parts:

$$\frac{\partial c}{\partial t} + \nabla \cdot \boldsymbol{f}(c) = 0$$

$$\frac{\partial c}{\partial t}\Phi_{i,j} + \nabla \cdot \boldsymbol{f}(c)\Phi_{i,j} = 0$$

$$\int_{\mathcal{K}_i} \frac{\partial c}{\partial t}\Phi_{i,j}\,dV + \int_{\mathcal{K}_i} \nabla \cdot \boldsymbol{f}(c)\Phi_{i,j}\,dV = 0 \qquad (4.2)$$

$$\int_{\mathcal{K}_i} \frac{\partial c}{\partial t}\Phi_{i,j}\,dV + \int_{\partial\mathcal{K}_i} (\boldsymbol{f}(c)\cdot\boldsymbol{n})\Phi_{i,j}\,dA - \int_{\mathcal{K}_i} \boldsymbol{f}(c)\nabla\Phi_{i,j}\,dV = 0.$$

Considering that the cell's surface $\partial\mathcal{K}_i$ consists of internal or boundary edges $\{\mathcal{E}_{i,e}\}_{e=1,\dots,E_i}$ we can rewrite 4.2 as

$$\int_{\mathcal{K}_i} \frac{\partial c}{\partial t}\Phi_{i,j}\,dV + \sum_{e=1}^{E_i}\int_{\mathcal{E}_{i,e}} (\boldsymbol{f}(c)\cdot\boldsymbol{n})\Phi_{i,j}\,dA - \int_{\mathcal{K}_i} \boldsymbol{f}(c)\nabla\Phi_{i,j}\,dV = 0. \qquad (4.3)$$

4.1.2 Numerical Fluxes

As the concentration c is unknown, we need to introduce a modal approximation

$$c(\mathbf{x},t)\,|_{\mathcal{K}_i} \approx \bar{c}(\mathbf{x},t)\,|_{\mathcal{K}_i} = c_i(x,t) = \sum_{k=0}^{M} c_{i,k}(t)\Phi_{i,k}(\mathbf{x}) \qquad (4.4)$$

with the Galerkin approach of identical Ansatz and test functions. For we do not enforce continuity on $\mathcal{E}_{i,e}$ and thus

$$c_i\,|_{\mathcal{E}_{i,e}} =: c^- \neq c^+ := c_{n(i,e)}\,|_{\mathcal{E}_{i,e}} \qquad (4.5)$$

we cannot simply insert the approximation into equation (4.3). Therefore we will introduce a monotone, Lipschitz continuous numerical flux function $f = f(c^-, c^+, \mathbf{n}) : \mathbb{R}^{D+2} \to \mathbb{R}$ satisfying the consistency property

$$f(c^-, c^+, \mathbf{n}) = -f(c^-, c^+, -\mathbf{n}). \tag{4.6}$$

By including these definitions into (4.3) we receive

$$\int_{\mathcal{K}_i} \frac{\partial c_i}{\partial t} \Phi_{i,j} \, dV + \underbrace{\sum_{e=1}^{E_i} \int_{\mathcal{E}_{i,e}} f\left(c^-, c^+, \mathbf{n}\right) \Phi_{i,j} \, dA - \int_{\mathcal{K}_i} \boldsymbol{f}\left(c_i\right) \cdot \nabla \Phi_{i,j} \, dV}_{=:(\mathbf{f_i})_j} = 0 \tag{4.7}$$

with the discrete operator $\mathbf{f_i} = \mathbf{f_i}(t, \mathbf{c_i}) \in \mathbb{R}$.

Some well-known examples of numerical fluxes contain [2]:

- The Godunov flux

- The Engquist-Osher flux

- The Lax-Friedrichs flux

- The local Lax-Friedrichs flux

- The Roe flux with 'entropy flux',

whereby we will attend to the local Lax-Friedrichs or Rusanov flux, which is defined as

$$f(c^-, c^+, \mathbf{n}) = \frac{\mathbf{f}(c^-) + \mathbf{f}(c^+)}{2} \cdot \mathbf{n} - \frac{C_R}{2}(c^+ - c^-) \tag{4.8}$$

with the coefficient C_R based on a local stability criterion. In this thesis we will use an estimate based on the maximum local wave speed

$$C_R = \max(|\mathbf{u}^+ \cdot \mathbf{n}| + a^-, |\mathbf{u}^- \cdot \mathbf{n}| + a^+) \tag{4.9}$$

with $u^\pm$ and $a^\pm$ denoting the normal velocity and the local speed of sound at the edges. As the Rusanov flux has a high stability it will be used disregarding that it is prone to numerical diffusion.

4.2 RK Time Discretization

After having studied the spatial discretization, we will now attend to the time discretization, using the RK method.

First of all, we need to reformulate equation (4.7) in order to achieve a system of coupled ordinary differential equation (ODE)s.

$$\int_{\mathcal{K}_i} \frac{\partial c_i}{\partial t} \Phi_{i,j} \, dV + \underbrace{\sum_{e=1}^{E_i} \int_{\mathcal{E}_{i,e}} f\left(c^-, c^+, \mathbf{n}\right) \Phi_{i,j} \, dA - \int_{\mathcal{K}_i} f\left(c_i\right) \cdot \nabla \Phi_{i,j} \, dV}_{=:(\mathbf{f_i})_j} = 0.$$

The first term of the equation above can be reformulated as

$$\int_{\mathcal{K}_i} \frac{\partial c_i}{\partial t} \Phi_{i,j} \, dV = \int_{\mathcal{K}_i} \frac{\partial}{\partial t} \left(\sum_{k=0}^{M} c_{i,k}(t) \Phi_{i,k}(\mathbf{x}) \right) \Phi_{i,j} \, dV$$

$$= \sum_{k=0}^{M} \frac{\partial c_{i,k}}{\partial t} \underbrace{\int_{\mathcal{K}_i} \Phi_{i,k} \Phi_{i,j} \, dV}_{=:(\mathbf{M_i})_{k,j}}$$

$$= \mathbf{M_i} \frac{\partial \mathbf{c_i}}{\partial t}$$

thus leading to

$$\mathbf{M_i} \frac{\partial \mathbf{c_i}}{\partial t} + \mathbf{f_i} = 0 \tag{4.10}$$

with $\mathbf{M_i} \in \mathbb{R}^{M,M}$ being a cell-local symmetric mass matrix associated with $\mathcal{K}_i$. As we have assumed an orthonormal basis $\left\{ \Phi_{i,j} \right\}_{j=1,...,M}$ thus reducing the mass matrix to the identity matrix I, the ODEs simplify to

$$\frac{\partial \mathbf{c_i}}{\partial t} + \mathbf{M_i}^{-1} \mathbf{f_i} = \mathbf{0} \tag{4.11}$$

$$\frac{\partial \mathbf{c_i}}{\partial t} + \mathbf{f_i} = \mathbf{0}. \tag{4.12}$$

Using an explicit RK method of order S we can now advance this system of ODEs and calculate the new coefficients from

$$\mathbf{c_i}(t_1) = \mathbf{c_i}(t_0) - \Delta t \sum_{s=1}^{S} (\alpha)_\mathbf{s} \mathbf{k_s}, \tag{4.13}$$

with a known solution at t_0 to a new instant t_1 and $\Delta t = t_1 - t_0$, where

$$\mathbf{k}_s = \mathbf{f}_i \left(t_0 + (\beta)_s \Delta t, \mathbf{c}_i(t_0) + \Delta t \sum_{t=1}^{S} (\mathbf{\Gamma})_{s,t} \mathbf{k}_t \right). \tag{4.14}$$

The coefficients $\alpha \in \mathbb{R}^S$, $\beta \in \mathbb{R}^S$ and $\Gamma \in \mathbb{R}^S$ are specific for each RK method. Those of the most common RK methods are displayed in the Butcher Tableaus in 4.2. They determine the stability and accuracy of the time integration scheme.

$$
\begin{array}{c|cccccc}
0 & & & & & \\
\beta_2 & \Gamma_{21} & & & & \\
\beta_3 & \Gamma_{31} & \Gamma_{32} & & & \\
\vdots & \vdots & \vdots & \ddots & & \\
\beta_s & \Gamma_{s1} & \Gamma_{s2} & \cdots & \Gamma_{s,s-1} & \\
\hline
 & \alpha_1 & \alpha_2 & \cdots & \alpha_{s-1} & \alpha_s
\end{array}
$$

Table 4.1.: Butcher Tableau for the Explicit Runge–Kutta Method.

A well-known stability criterion according the explicit Euler time discretization for linear, hyperbolic PDEs, namely the Courant-Friedrichs-Lewy (CFL) criterion, restrains the temporal step-size Δt:

$$\Delta t \leq c_{CFL} \frac{h}{\underline{u}} \tag{4.15}$$

$$
\begin{array}{c|c}
0 & \\
\hline
 & 1
\end{array}
\qquad
\begin{array}{c|cc}
0 & & \\
1 & 1 & \\
\hline
 & \frac{1}{2} & \frac{1}{2}
\end{array}
\qquad
\begin{array}{c|ccc}
0 & & & \\
\frac{1}{3} & \frac{1}{3} & & \\
\frac{2}{3} & 0 & \frac{1}{3} & \\
\hline
 & \frac{1}{4} & 0 & \frac{3}{4}
\end{array}
\qquad
\begin{array}{c|cccc}
0 & & & & \\
\frac{1}{2} & \frac{1}{2} & & & \\
\frac{1}{2} & 0 & \frac{1}{2} & & \\
1 & 0 & 0 & 1 & \\
\hline
 & \frac{1}{6} & \frac{2}{6} & \frac{2}{6} & \frac{2}{6}
\end{array}
$$

| Explicit Euler (first order) | Trapezoidal rule (second order) | Third order TVD (third order) | Classical RK (fourth order) |

Table 4.2.: Butcher Tableaus for different orders of RK

with $\underline{u} \in \mathbb{R}^+$ denoting the largest propagation velocity and a positive constant $c_{CFL} \leq 1$ depending on the applied spatial discretization procedure.

Concerning the Euler equations the largest propagation velocity is given by $\underline{u} = ||\mathbf{u}|| + a$ and by taking the influence of the approximation order P into account we can use

$$\Delta t \leq \frac{c_{CFL}}{2P+1} \frac{h}{||\mathbf{u}|| + a} \tag{4.16}$$

as a sufficiently accurate estimate for the stability criterion in this thesis.

5 The Immersed Boundary Method

In the following chapter we will study the DG method with immersed boundaries. IBMs are characteristic in the way of creating the calculation mesh as they do not rely on body fitted grids but on a level set function φ that cuts the cells into the physical and the void region. It therefore makes the mesh generation much easier, as it only needs a cartesian mesh and a function that approximates the level set. Brought along with the cartesian mesh, it is easily parallelisable, thus rendering it convenient for more complex structures that shall be computed on several processors.

5.1 The DG Scheme with Immersed Boundaries

We regard an implicit representation of an immersed boundary using the level set function φ that parts the calculation area Ω_h into @TODO: align

the physical region $\mathcal{A} = \{\vec{x} \in \Omega_h : \varphi(\vec{x}) > 0\}$,

the void region $\mathcal{B} = \{\vec{x} \in \Omega_h : \varphi(\vec{x}) < 0\}$,

and the immersed boundary $\mathcal{I} = \{\vec{x} \in \Omega_h : \varphi(\vec{x}) = 0\}$.

In our next step we use the definitions above in 4.7 considering cell $\mathcal{K}_i$ with the sub-domain $\mathcal{A}_i = \mathcal{K}_i \cap \mathcal{A}$ and the surface $\partial \mathcal{A}_i$. As in cut cells the surface $\partial \mathcal{A}_i$ consists not only of the edges $\left\{ \mathcal{E}_{i,e}^{\mathcal{A}} \right\}_{e=1,\dots,E} = \left\{ \mathcal{E}_{i,e} \cap \bar{\mathcal{A}}_i \right\}_{e=1,\dots,E}$ but also of the boundary segment $\mathcal{I}_i = \mathcal{K}_i \cap \mathcal{I}$, the discrete weak formulation using an IBM follows as

$$\int_{\mathcal{A}_i} \frac{\partial c_i}{\partial t} \Phi_{i,j} \, dV + \sum_{e=1}^{E_i} \int_{\mathcal{E}_{i,e}^{\mathcal{A}}} f\left(c^-, c^+, \mathbf{n}\right) \Phi_{i,j} \, dA + \int_{\mathcal{I}_i} f\left(c^-, c^+, \mathbf{n}_{\mathcal{I}}\right) \Phi_{i,j} \, dA - \int_{\mathcal{A}_i} \boldsymbol{f}\left(c_i\right) \cdot \nabla \Phi_{i,j} \, dV = 0$$

(5.1)

with $\mathbf{n}_{\mathcal{I}} = -\dfrac{\nabla \varphi}{\|\nabla \varphi\|}$. In intersected cells the mass matrix is defined by

$$(\mathbf{M_i})_{k,j} := \int_{\mathcal{A}_i} \Phi_{i,k} \Phi_{i,j} \, dV$$

(5.2)

and the discrete operator by

$$(\mathbf{f}_i)_j := \sum_{e=1}^{E_i} \int_{\mathcal{E}_{i,e}^{\mathcal{A}}} f\left(c^-, c^+, \mathbf{n}\right) \Phi_{i,j}\, dA + \int_{\mathcal{I}_i} f\left(c^-, c^+, \mathbf{n}_{\mathcal{I}}\right) \Phi_{i,j}\, dA - \int_{\mathcal{A}_i} \boldsymbol{f}\left(c_i\right) \cdot \nabla \Phi_{i,j}\, dV. \qquad (5.3)$$

The difficulty of the IBM lies in the correct evaluation of $\mathcal{A}_i$ and $\mathcal{I}_i$ and in the agglomeration of intersected cells with very small volume fractions

$$\mathrm{frac}(\mathcal{A}_i) = \frac{\mathrm{meas}(\mathcal{A}_i)}{\mathrm{meas}(\mathcal{K}_i)} \qquad (5.4)$$

as we will discuss in section 5.3.

5.2 RK Time Discretisation with Immersed Boundaries

In this thesis we only use explicit Euler time discretisation for immersed boundary problems as it is less computationally expensive than higher order RK:

$$\mathbf{c_i}(t_1) = \mathbf{c_i}(t_0) - \Delta t \mathbf{M}_i^{-1} \mathbf{f}_i(c). \qquad (5.5)$$

Using IBMs we have to modify the stability criterion and therefore use the modified step restriction

$$\Delta t \leq \frac{c_{CFL}}{2P+1} \frac{\sqrt[D]{\mathrm{meas}(\mathcal{A}_i)}}{\|\mathbf{u}\| + a} \qquad (5.6)$$

which is strongly influenced by the sub-cell $\mathcal{A}_i$ with the smallest volume.

5.3 Cell Agglomeration

As can be seen in 5.6 the time step size is strongly restricted in cells with very small volume fractions. This leads to an elongated calculation process thus rendering the method impractical. Therefore we need to agglomerate those small cells to larger ones using a cell agglomeration factor $0 \leq \alpha \leq 1$.

The cell agglomeration strategy depends on finding the source cells $\left\{\mathcal{K}_s^{\mathrm{src}}\right\}_{s=1,\dots,S}$ with $\mathrm{frac}(\mathcal{A}_i) \leq \alpha$ and agglomerating them to the neighboring cell with the highest volume fraction, namely target cell $\mathcal{K}_s^{\mathrm{tar}}$.

For the neighboring cells are weakly coupled via fluxes, the basis $\vec{\Phi}_i$ can be extended from the target cell into the source cell. Therefore the source cell can formally be deleted from the discretisation mesh, reducing it to $\left\{\mathcal{K}_s^{\mathrm{agg}}\right\}_{i=1,\ldots,N-S}$. As can be found in @TODO: paper zitieren, it however does not reflect the actual implementation in BoSSS which only requires few cell-local matrix-vector products per time-step, thus not affecting the parallel efficiency. @TODO: Bilder aus paper, beschreiben

6 Validation of BoSSS Concerning Euler Equations with IBMs

In the following chapter we will regard a flow at Mach 0.2 around a frictionless cylinder with adiabatic slip walls at changing parameters such as the polynomial degree, the mesh size and the position of the cylinder in order to validate BoSSS with immersed boundaries concerning robustness and convergence.

During the simulation we compute only half of the domain with $-40 \leq x \leq 40$, $0 \leq y \leq 40$ and the cylinder radius $r = 1$ as the flow above and below the cylinder should be identical.

6.1 Robustness Study

In the first study regarding the frictionless cylinder, we compare the absolute error of entropy for a polynomial degree from 1 to 3 along a shift of the centre point of the cylinder from -0.075 to 0.075 at steps of 0.015. By shifting the cylinder we can consider several cases where the cells would be cut differently and therefore cause different cell agglomerations. The cell agglomeration threshold is at a constant level of 0.5 in a mesh of 32×32 cells. In this example we aim at proving the robustness of the solver as for each position of the cylinder the error of entropy should not vary too much thus making it independent of the way the border cells are cut.

As we look at the chart 6.1, first of all we will note that the absolute error of entropy decreases with increasing polynomial degree. As a higher polynomial degree implies a better approximation this can be explained very easily.

Secondly, we can observe that the error of entropy behaves roughly symmetrically to the ordinate. As we shifted the cylinder symmetrically this observation does not surprise us either.

For degree 1 and 2 the error is at a fairly constant value throughout the cylinder shift; at the polynomial degree 3 it is very irregular. The two most discordant values appeared at a shift of ± 0.03. There the calculation was cancelled early because of illegal values for momentum. I tried getting them to work by reducing the time step size and increasing the node count safety factor that should produce a more stable calculation, but the calculation never came to the convergence criterion.

We can therefore infer that with increasing polynomial degree at a mesh that course the calculation gets very instable; a finer mesh should be used.
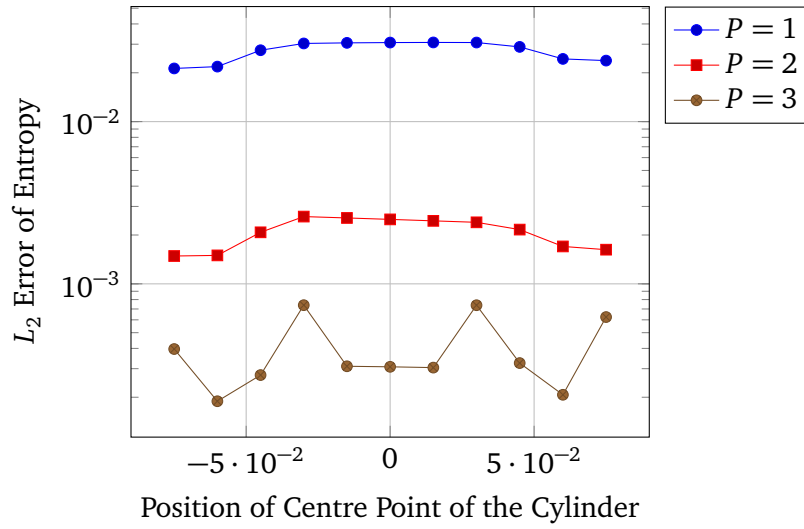
Figure 6.1.: Convergence Plot

Now for rough explication why the results are different for different meshes we will consider two cases which have the largest error difference apart from degree 3: degree 2 at the shifts −0.06 and −0.03.
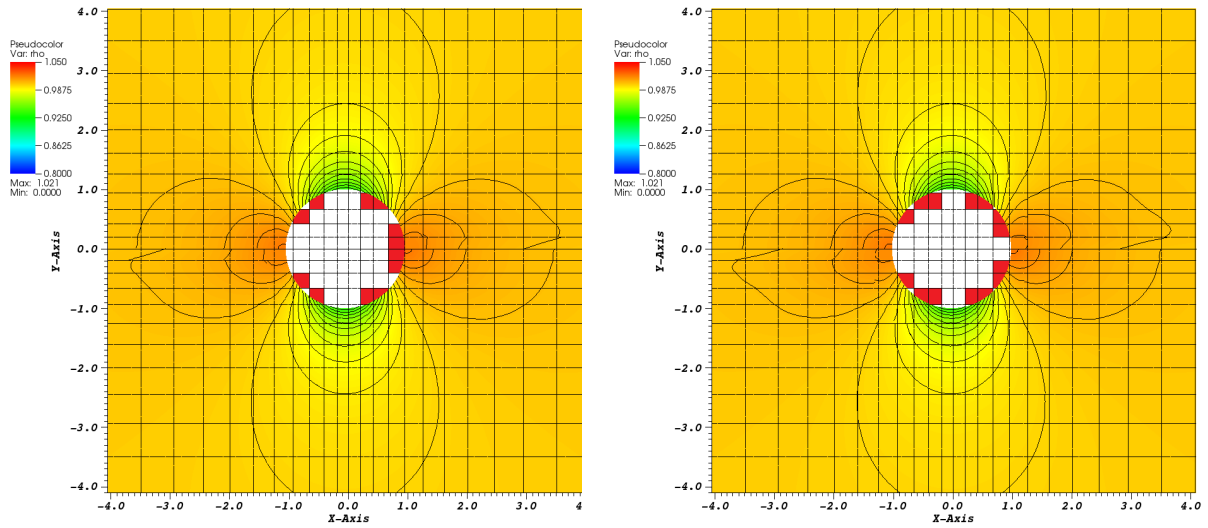
Degree 2, shift −0.06   Degree 2, shift −0.03

Figure 6.2.: Isolines of pressure

In figure 6.2 you can see the two mentioned cases with highlighted isolines of pressure and pseudocolored density. As only the upper half of the cylinder has been calculated, I reflected the results through the centre point of the cylinder. Therefore you can easily see that the results

are not flawless, as the flow before and after the obstacle should be identical. Furthermore you can see that in the left picture the isolines are smoother than in the right one. In order to give an explanation for the higher error of entropy in the former I highlighted the cells that should have been agglomerated in red. In the left case there are less agglomerated cells than in the right one, therefore there was a not so big agglomeration mistake made.

@TODO: bessere Erklärung für Agglomerationsfehler

Except for the polynomial degree 3, the error of entropy changes very little for the different cases. We can therefore assume that the solver is good enough validated concerning the way the agglomerated cells influence the calculation as long as we consider a fine enough mesh for higher degrees.

6.2 Convergence Study of Mesh Size and Polynomial Degree

In the second study we vary the mesh size of our geometry from 32×32 by 64×64 to 128×128 cells. Additionally we also vary the polynomial degree from 0 to 4, consequently regarding fifteen cases in total.

Our aim is the validation of the convergence of the RKDGM based solver for the inviscid cylinder. Therefore we hope to achieve an experimental order of convergence that is near the optimal rate $O(h^{P+1})$. In chart 6.3 I compared the absolute error entropy to the mesh size logarithmically for each polynomial degree.

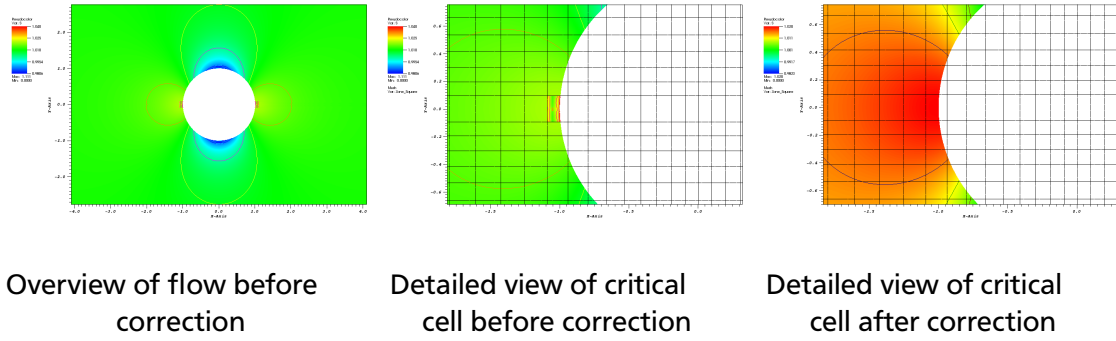As you can see in 6.3 each graph has a quite constant gradient that is higher with in-
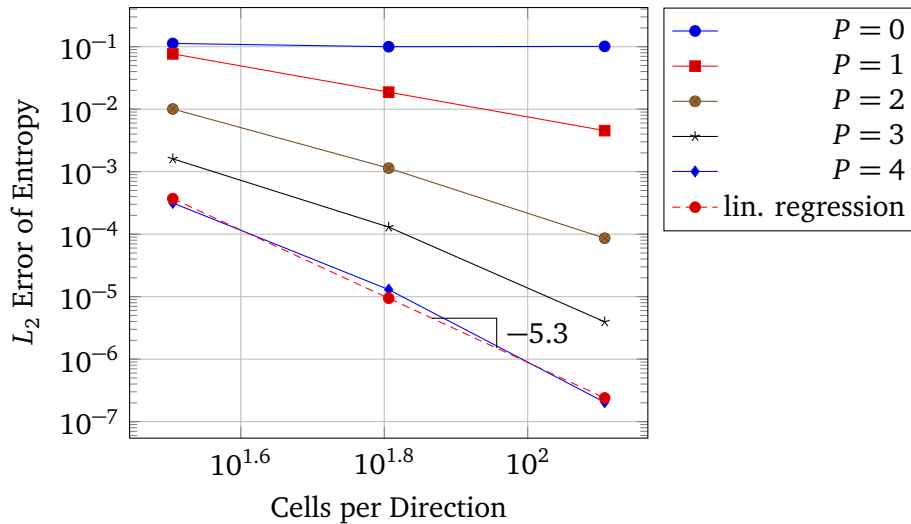
Figure 6.3.: Convergence Plot

creasing polynomial degree which is approximately of the order $P + 1$ as we hoped. For the calculation with higher polynomial degrees it was necessary to adjust time step size and node

count safety factor again in order to get the calculation to terminate.

As an example for the correction of a critical calculation I visualised the case with mesh size 128×128 and polynomial degree $P = 3$ before and after the correction in 6.4. Again, I visualised entropy and pressure. The picture in the middle shows a zoomed view of the critical cell where a high amount of entropy was produced and lead to the breakup. Please remark that differently coloured entropy ranges had to be used before and after the correction in order to point out the critical cell.

| Overview of flow before correction | Detailed view of critical cell before correction | Detailed view of critical cell after correction |

Figure 6.4.: Mesh size 128×128, $P = 3$

6.3 Conclusion

After having studied the behaviour of BoSSS concerning the Euler equations with immersed boundaries, we can conclude that is sufficiently validated. The robustness studied showed that the results are mostly independent from the exact position of the grid cells. During the convergence study we remarked that the convergence behaves as desired with an order close to the optimal rate of $O(h^{P+1})$.

Nevertheless in order to receive the correct result it should always be guaranteed that the calculation can terminate properly which can be derived by a smaller CFL number, respectively time step size, an increased node count safety factor or smaller cells. Unfortunately these precautions cause a higher overall runtime.

7 The viscous cylinder

The flow around a viscous cylinder has been approached by many papers both experimentally and numerically, e.g. [3], [4], [5], though very few numerical approaches use a RKDG method combined with immersed boundaries. In order to verify the BoSSS code with immersed boundaries not only for the Euler equations as we did in chapter 6 but also for the viscous case we will now consider different Reynolds numbers for the steady and unsteady flow and compare our results to those of other studies.

7.1 Theory

The flow around a viscous cylinder can be divided into different sections depending on the Reynolds number as shown in 7.1. The first section applies for Reynolds numbers $0 < \text{Re} < 40 - 50$ characterised by a laminar steady flow. In that regime a recirculation region with two symmetric vortices with opposite directions is comprised by the wake. The flow can be described using the wake separation length W^*.

The second section contains all other Reynolds number $\text{Re} > 40 - 50$ and thus describes
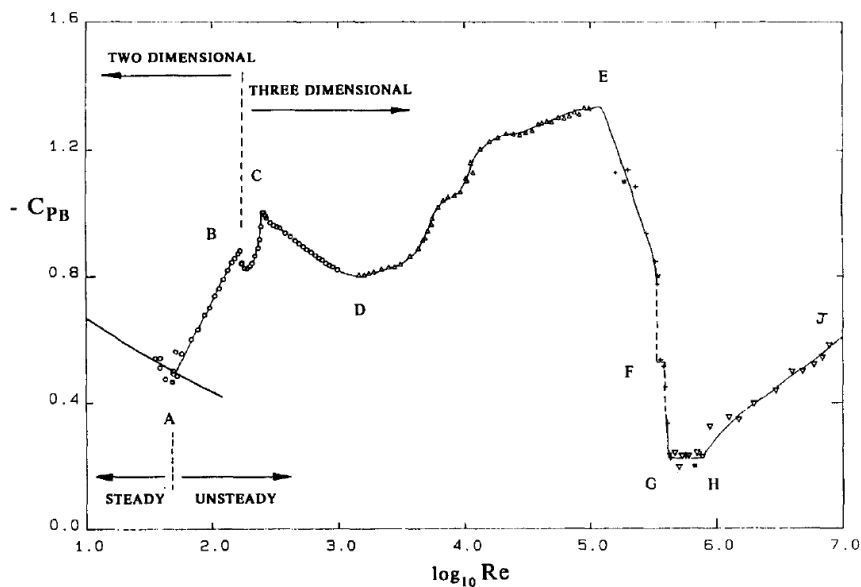

Figure 7.1.: Overview of Base Suction Coefficients over Reynolds Number [3]

the unsteady flow. It can be subdivided in several subsections [3]:

$40 - 50 < \text{Re} < 190$ laminar vortex shedding,

190 < Re < 260 3D wake-transition regime,

260 < Re < 1000 increasing disorder in the fine-scale three dimensionalities,

1000 < Re < 200000 shear layer transition regime,

200000 < Re critical transition, supercritical regime and post-critical regime.

As we will only discuss Reynolds numbers up to Re = 200 the important phases for us are the laminar steady regime and the laminar vortex shedding. At around Re = 190 the three dimensionality of the system has an incrementing influence on the flow; for we only analyse the 2-D model of the experiment we stop at Re = 200 expecting slight deflection in our results.

7.1.1 The Laminar Steady Regime

At Reynolds numbers below 50 the flow forms a steady recirculation region, characterised by the wake separation length W^*. It is built by two symmetrically placed vortices on each side of the wake as can be seen in 7.2. It has been shown experimentally as well as numerically, that the wake separation length increases with increasing Reynolds number.
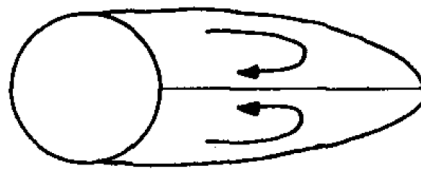

STEADY WAKE

Figure 7.2.: Recirculation Region [3]

7.1.2 Laminar Vortex Shedding

For Reynolds numbers of between 50 and 200 the recirculation region develops instabilities leading to the development of turbulence in the wake. This results into fully periodic vortex shedding, known as the Kármán vortex street, as can be seen in 7.3. With increasing Reynolds number the amplitudes of drag and lift coefficients increases while the Strouhal number, respectively frequency, decreases.

UNSTEADY WAKE
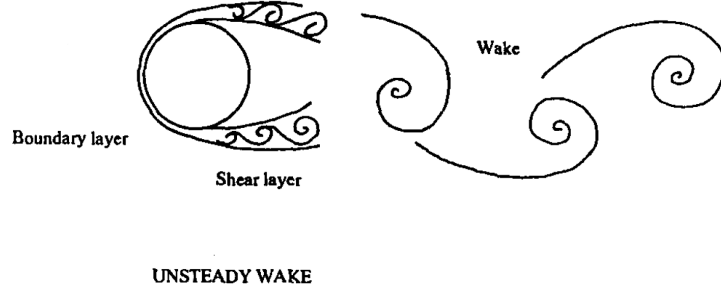
Figure 7.3.: Kármán Vortex Street [3]

7.2 Simulations

In this section we will compare the lift and drag coefficients at different Reynolds numbers and mesh sizes at a constant agglomeration threshold of 0.1, different polynomial degrees of 1, 2 and 3 and meshes of 40 × 40, 80 × 80 and 160 × 160 cells. These mesh sizes were developed from 32, 64 and 128 cells per direction but overlaying them with a mesh with one eighth of those in order to better approach the boundary layer of the cylinder. The meshes can be found in the appendix.

The different simulation properties will be abbreviated as DG + *polynomial degree* + MS + *number of cells per direction*, e.g. DG2MS80 for a simulation with polynomial degree 2 and 80 × 80 cells.

The drag and lift coefficients C_D and C_L are defined as

$$C_D = \frac{d}{q_\infty L_\infty} \tag{7.1}$$

$$C_L = \frac{l}{q_\infty L_\infty} \tag{7.2}$$

with the dynamic pressure $q_\infty = \frac{1}{2}\rho_\infty V_\infty^2$. For we set $L_\infty = \rho_\infty = V_\infty = 1$ in our boundary and initial conditions, we can assume

$$C_D = 2 \cdot d \tag{7.3}$$

$$C_L = 2 \cdot l, \tag{7.4}$$

with the drag and lift forces d and l provided from the calculation.

During the simulations we now compute the complete domain with $-40 \leq x \leq 40$, $-40 \leq y \leq 40$ and the cylinder radius $r = 1$ as we expect asymmetrical oscillations of the flow with higher Reynolds numbers. We will use a rectilinear mesh that is finer near the cylinder, an isothermal wall boundary condition at the cylinder wall and supersonic inlet boundary condi-

tions for the domain borders that shall prevent the reflection of the initial wave.

For the calculation with DG3MS40 no results could be found. The case produces a ill conditioned matrix that is not positive definite; thus the Cholesky factorisation fails. We can therefore conclude that it is unsafe to use BoSSS with high order on very coarse meshes. These results match those that we found in 6 where we got irregular values for DG3MS32 during the robustness study.

7.2.1 Steady State Simulations (Re < 40 − 50)

For the steady state simulations we can use the wake separation length W^* as an additional variable to compare to other simulations. It can be found from examining the x-velocity U at
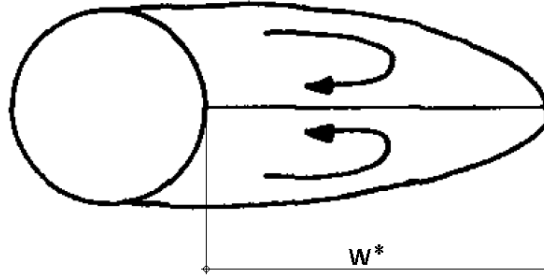
Figure 7.4.: Wake separation length, from [3] modified

$y = 0$; the x-position where U changes its sign should be the end position of the wake.

Simulation at Reynolds Number 20

We will now simulate the flow at Re $= 20$ and compare our results to several experimental and numerical results as shown in 7.1. The results are divided into three categories: experimental, numerical incompressible and numerical compressible in order to coincide with the arrangement given by [6].

Simulation at Reynolds Number 40

7.2.2 Unsteady Simulations (Re > 40 − 50)

In order to compare the unsteady simulations we need the Strouhal number

$$St = \frac{f\,L_\infty}{V_\infty}. \tag{7.5}$$

Re = 20	Source	2D/3D	W^*	C_D
Numerical - Incompressible	Dennis et al [1970]	2D	0.94	2.05
	Forberg [1980]	2D	0.91	2.00
	Linnick et al. [2005]	2D	0.93	2.06
Experimental	Coutanceau et al. [1978]	-	0.93	-
	Tritton [1959]	-	-	2.09
Numerical - Compressible	Brehm et al. [2015] (Ma = 0.1)	3D	0.96	2.02
	Ayers [2015]	2D	0.975	2.06
	Present Results:	2D	d	4

Table 7.1.: Comparison of Results for W^* and C_D, from [6] modified

C_D		MS		
		40	80	160
DG	1			
	2			
	3			

Table 7.2.: C_D Values for each simulation

W^*		MS		
		40	80	160
DG	1			
	2			
	3			

Table 7.3.: Wake Separation Lengths for each simulation
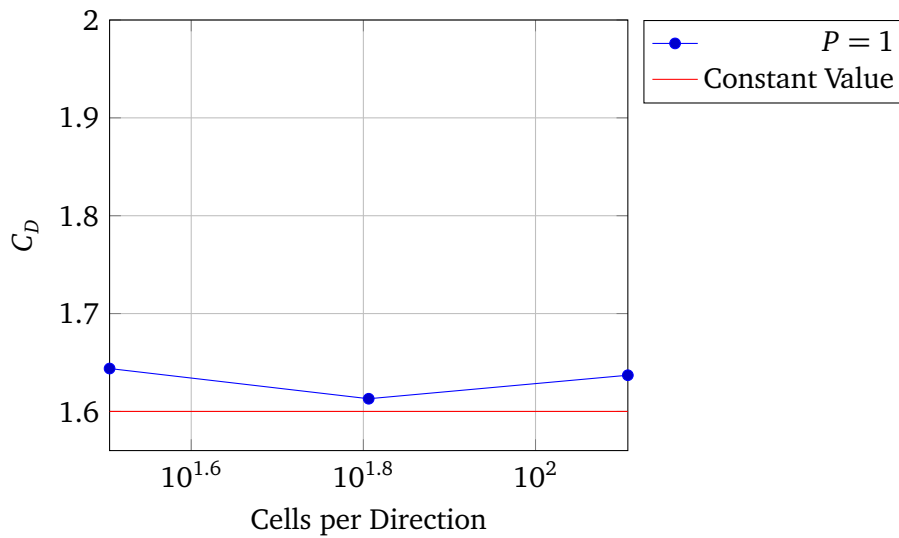
Figure 7.5.: Convergence Plot

Re = 40	Source	2D/3D	W^*	C_D
	Dennis et al [1970]	2D	2.35	1.52
Numerical - Incompressible	Forberg [1980]	2D	2.24	1.50
	Linnick et al. [2005]	2D	2.28	1.54
	Coutanceau et al. [1978]	-	2.13	-
Experimental	Tritton [1959]	-	-	1.59
	Brehm et al. [2015] (Ma = 0.1)	3D	2.26	1.51
Numerical - Compressible	Ayers [2015]	2D	2.250	1.605
	Present Results:	2D	d	4

Table 7.4.: Comparison of Results for W^* and C_D, @TODO: modified Lawrence

As our initial and boundary conditions give $V_\infty = L_\infty = 1$, we can calculate St $= f$ with f found from examining the oscillation of C_L over time. For developing vortex shedding, the flow needs small perturbations that destabilize the flow towards a symmetry breaking state [4]. In reality those are given by the structure of the cylinder, the influence of the walls or the not completely straight inflow; in our simulations they come from small truncation errors and the computer's round-off errors. In order to accelerate the process until the wake begins to oscillate one could also start the flow with a vortex that induces a high perturbation much earlier. For it did not take long until the wake began to oscillate it was not needed in our simulations.

Simulation at Reynolds Number 100
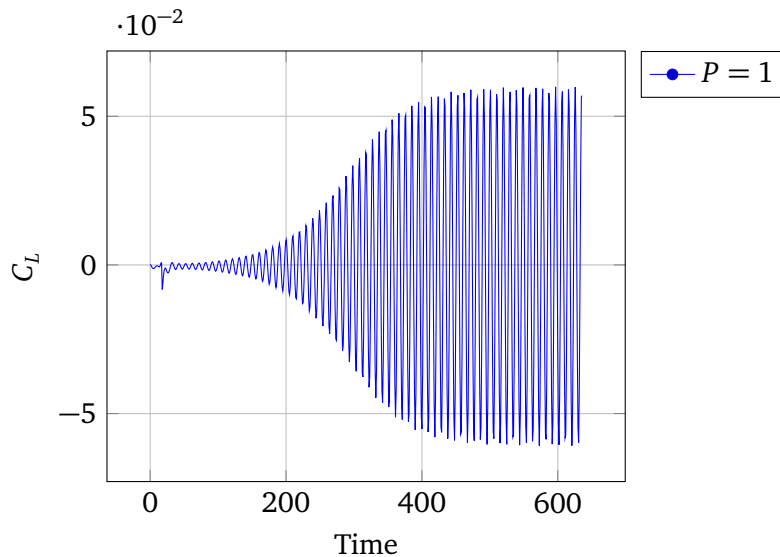
Figure 7.6.: Convergence Plot

Simulation at Reynolds Number 200

Re = 100	Source	2D/3D	St	C_D	C_L
Numerical - Incompressible	Gresho et al. [1984]	2D	0.18	1.76	-
	Linnick et al. [2005] ($\lambda = 0.056$)	2D	0.169	1.38 ±010	±337
	Linnick et al. [2005] ($\lambda = 0.023$)	2D	0.169	1.34 ±009	±333
	Persillon et al. [1998]	2D	0.165	1.253	-
	Saiki et al. [1996]	2D	0.171	1.26	-
	Persillon et al. [1998]	3D	0.164	1.240	-
	Liu et al. [1998]	3D	0.165	1.35 ±012	±339
Experimental	Berger et al. [1972]	-	0.16-0.17	-	-
	Clift et al. [1978]	-	-	1.24	-
	Williamson [1996]	-	0.164	-	-
Numerical - Compressible	Brehm et al. [2015] (Ma = 0.1)	3D	0.165	1.32 ±01	±32
	Ayers [2015]	2D	0.167	1.371 ±011	±333
	Present Results:	2D	d	4	

Table 7.5.: Comparison of Results for St, C_D and C_L, @TODO: modified Lawrence
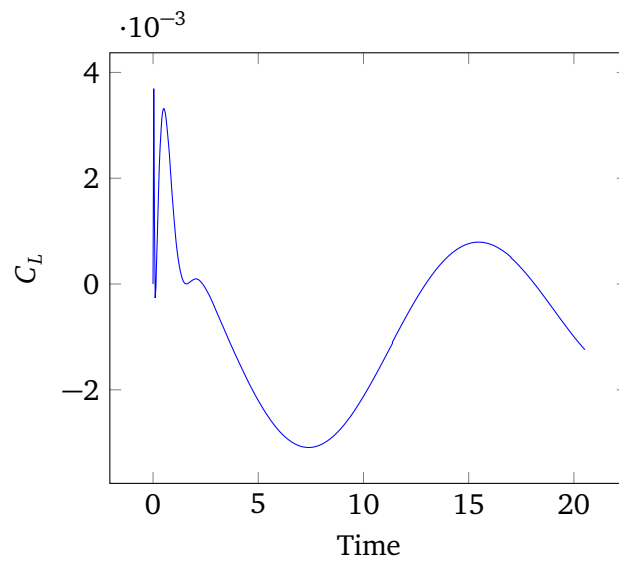
Figure 7.7.: Convergence Plot

Re = 100	Source	2D/3D	St	C_D	C_L
Numerical - Incompressible	Dennis et al [1970]	2D	0.94	2.05	
	Forberg [1980]	2D	0.91	2.00	
	Linnick et al. [2005]	2D	0.93	2.06	
Experimental	Coutanceau et al. [1978]	-	0.93	-	
	Tritton [1959]	-	-	2.09	
Numerical Compressible	Brehm et al. [2015] (Ma = 0.1)	3D	0.96	2.02	
	Ayers [2015]	2D	0.975	2.06	
	Present Results:	2D	d	4	

Table 7.6.: Comparison of Results for W^* and C_D, @TODO: modified Lawrence
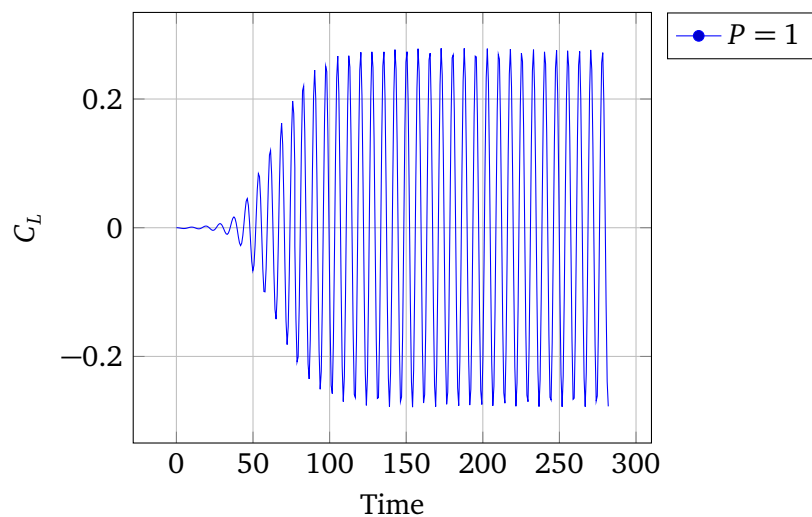
Figure 7.8.: Convergence Plot

8 Discussion

9 Bibliography

[1] MÜLLER, B., "Methods for higher order numerical simulations of complex inviscid fluids with immersed boundaries," 2014.

[2] COCKBURN, B., "Advanced numerical approximation of nonlinear hyperbolic equations: Lectures given at the 2nd session of the centro internazionale matematico estivo (c.i.m.e.) held in cetraro, italy, june 23–28, 1997," in, QUARTERONI, A., Ed. Berlin, Heidelberg: Springer Berlin Heidelberg, 1998, ch. An introduction to the Discontinuous Galerkin method for convection-dominated problems, pp. 151–268, ISBN: 978-3-540-49804-9. DOI: 10.1007/BFb0096353.

[3] WILLIAMSON, C. H., "Vortex dynamics in the cylinder wake," *Annual review of fluid mechanics*, vol. 28, no. 1, pp. 477–539, 1996.

[4] PERSILLON, H. and BRAZA, M., "Physical analysis of the transition to turbulence in the wake of a circular cylinder by three-dimensional navier–stokes simulation," *Journal of Fluid Mechanics*, vol. 365, pp. 23–88, Jun. 1998, ISSN: 1469-7645. DOI: 10.1017/S0022112098001116.

[5] CANUTO, D. and TAIRA, K., "Two-dimensional compressible viscous flow around a circular cylinder," *Journal of Fluid Mechanics*, vol. 785, pp. 349–371, 2015.

[6] AYERS, L. F., *Validation of a discontinuous galerkin based compressible cfd solver*, Dec. 2015.

List of Figures

List of Tables
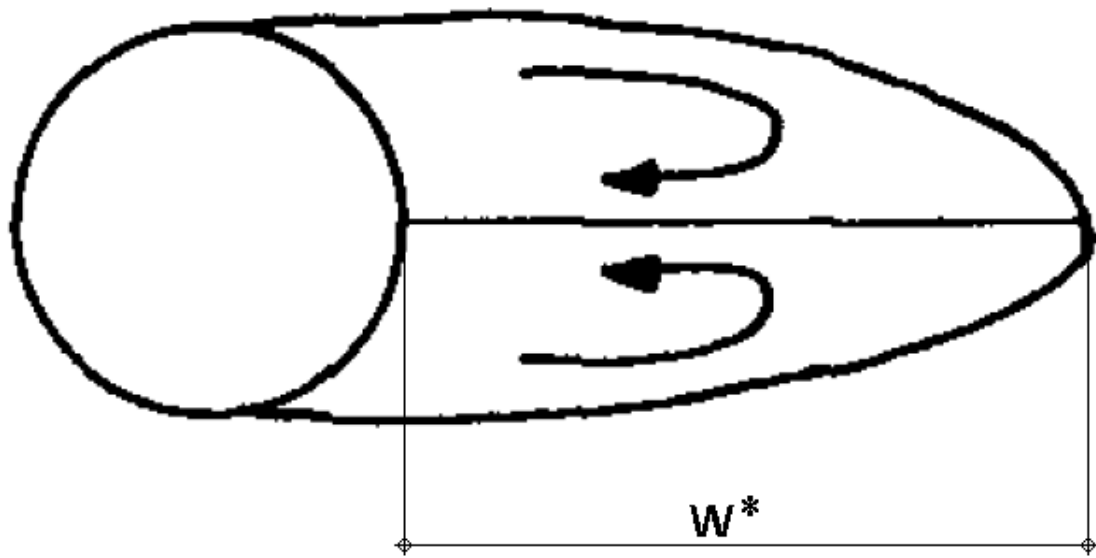
A Appendix

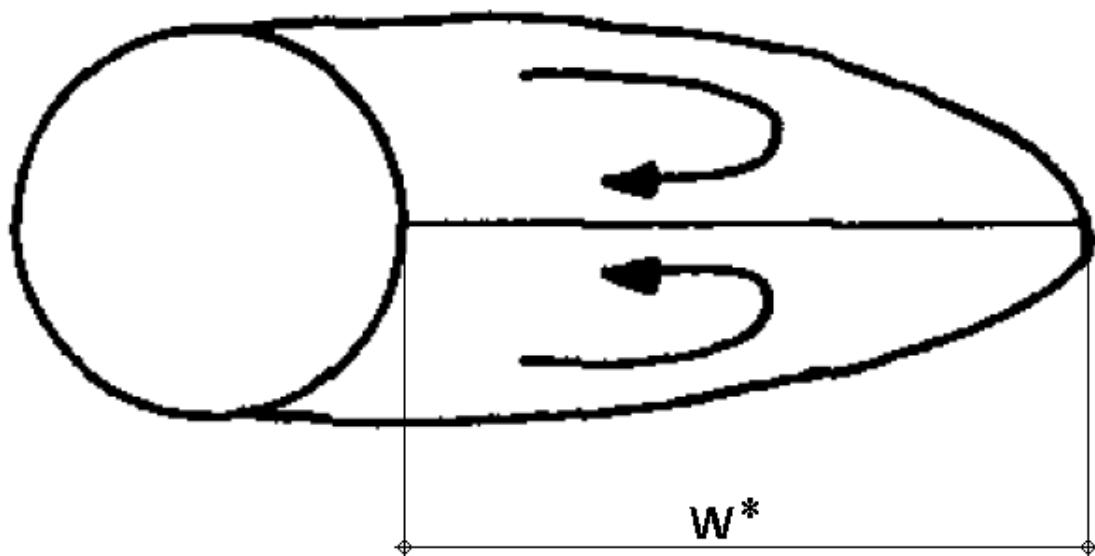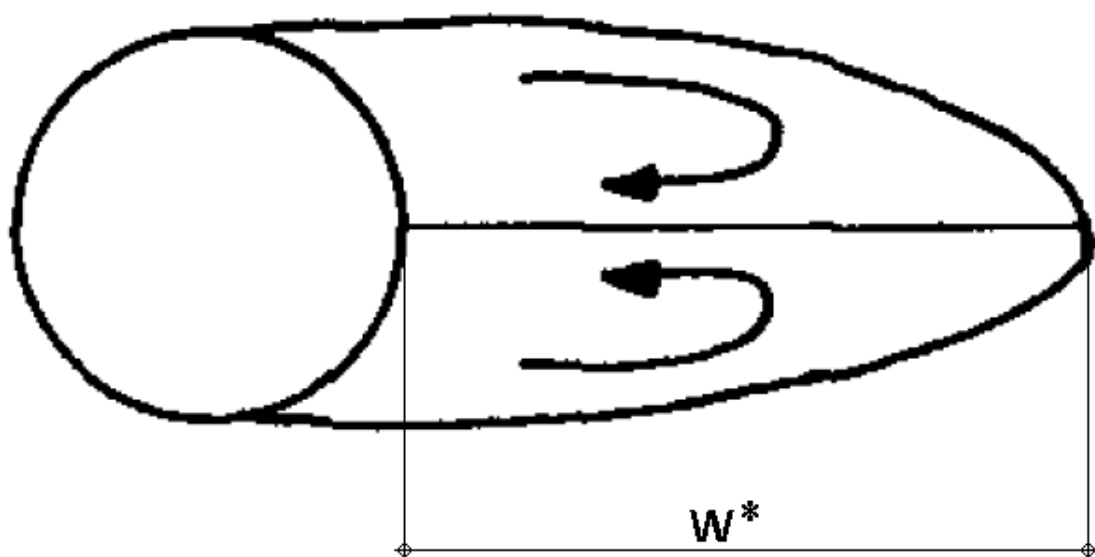## A.1 Mesh properties

Figure A.1.: Mesh for MS40

Figure A.2.: Mesh for MS80

Figure A.3.: Mesh for MS160